Effect of the Solid Phase on the Global Phase Behavior of Lennard–Jones Mixtures

Brian C. Attwood and Carol K. Hall
Dept. of Chemical Engineering, North Carolina State University, Raleigh, NC 27695

DOI 10.1002/aic.10157
Published online in Wiley InterScience (www.interscience.wiley.com).

Complete phase diagrams, that is, showing the solid, liquid, and vapor phases, are calculated for 29 binary mixtures of Lennard–Jones molecules characterized by different sets of interaction parameters using the Gibbs–Duhem integration technique. The impact of including the possibility of a solid phase on the global phase behavior of such mixtures is investigated by comparing the complete phase behavior calculated by simulation to the global phase diagram calculated from a fluid-phase-only equation of state. Complete phase diagrams from each region of the global phase diagram are presented and compared with the fluid-phase-only phase behavior for the same mixture. It is found that for mixtures in which the components have greatly dissimilar critical temperatures, the presence of the solid phase significantly alters the fluid-phase equilibria. In those cases, the phase behavior classification based on experimental observations should differ from that predicted by an equation-of-state approach. © 2004 American Institute of Chemical Engineers *AIChE J,* 50: 1948–1960, 2004

Keywords: phase diagram, Lennard–Jones mixtures, Gibbs–Duhem integration, critical temperature, equation of state

Introduction

Knowledge of the equilibria between solids and fluids is of vital importance in industrial processes based on crystallization, including separations, purification, concentration, solidification, and analysis. Crystallization is widely used in the pharmaceutical industry for product recovery because it yields high-purity products with a relatively low energy expenditure compared to that of distillation or other common methods of separation. Crystallization is also used in the desalination and decontamination of wastewater streams (Ericsson and Hallmans, 1996), the resolution of racemic mixtures (Schroer et al., 2001), and the separation and purification of numerous organic and inorganic mixtures (Kramer and Jansens, 2003). A prerequisite to efficient use of crystallization is knowledge of the solid–liquid phase equilibria of the components to be separated.

The techniques for calculating phase equilibria of a system based on knowledge of its equation of state are well established. Usually such calculations are carried out for specific values of the molecular interaction parameters to predict the phase equilibrium for a particular fluid or mixture. A different approach was taken in the late 1960s by van Konynenburg and Scott (van Konynenburg, 1968; van Konynenburg and Scott, 1970, 1980) who examined the phase behavior predicted for a binary mixture obeying the van der Waals equation of state over the entire range of interaction parameters. Their approach involved calculating the locus of critical points as a function of composition, pressure, and temperature. The type of phase behavior could then be classified into different types based on the projection of the locus of critical points onto the pressure–temperature (P– T) plane, as seen in Figure 1.

For their analysis of mixtures of equal-sized components, Scott and van Konynenburg (van Konynenburg, 1968; van Konynenburg and Scott, 1980) considered two dimensionless interaction parameters, ζ and Λ, which were a function of the attractive interaction parameters a_{11}, a_{22}, and a_{12} between molecules of components 1 and 2, where $\zeta = (a_{22} - a_{11})/(a_{22} + a_{11})$ and $\Lambda = (a_{11} + a_{22} - 2a_{12})/(a_{22} + a_{11})$. For equal-sized

Correspondence concerning this article should be addressed to C. K. Hall at hall@eos.ncsu.edu.

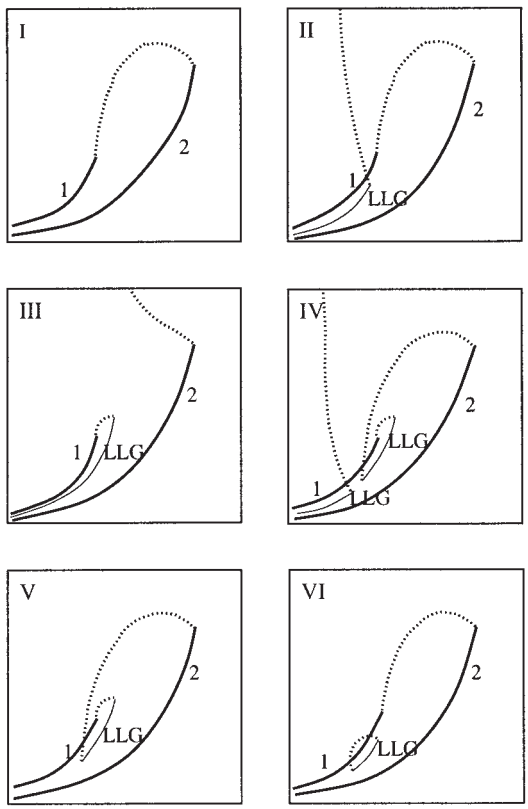

Figure 1. Six classifications of fluid-phase behavior.

The thicker lines are the boiling points of the pure fluids, the thinner lines represent three-phase coexistence, and the dotted lines are the loci of critical points.

molecules, ζ is related to the differences in critical temperatures or pressures of the pure components and Λ is related to the molar heat of mixing at $T = 0$. By determining the locus of critical points for a range of these parameters, they were able to construct a global phase diagram that divides the ζ– Λ parameter space into regions of similar phase behavior. Their global phase diagram for the van der Waals equation of state accounts for five of the six types of fluid-phase behavior known to exist in nature. The only type of phase behavior not found by Scott and van Konynenburg was type VI, which is distinguished from the other types by a region of closed-loop immiscibility. This was an important result because it showed that, even though the van der Waals equation of state is simplistic and quantitatively inaccurate for most fluids, it is able to predict much of the phase behavior found in nature.

Since that landmark article, a number of other groups have made similar explorations of the phase behavior for other equations of state. Furman et al. (1977) calculated the global phase behavior for a regular solution model of a three-component mixture that is nearly equivalent mathematically to a van der Waals model for binary mixtures, with the parameter b independent of concentration (implying that the molecules are of equal size) and the parameter a, a quadratic function of composition. They found significant agreement between the phase diagram they calculated and the one calculated by van Konynenburg and Scott for equal-diameter molecules. Later Furman and Griffiths (1978) revisited the global phase diagram for the van der Waals model and discovered a heretofore unidentified "shield region," a small region containing several new classes of phase behavior that had not been pointed out previously by van Konynenburg and Scott.

Mazur and Boshkov (Boshkov, 1987; Boshkov and Mazur, 1986; Mazur et al., 1985) investigated the global phase behavior of binary Lennard–Jones (L-J) fluid mixtures using a polynomial form for the equation of state that was proposed earlier and regressed to simulation data by Ree (1980). This was the first analysis of the phase behavior of a relatively modern equation of state that included a systematic look at the entire interaction parameter space. Mazur and Boshkov's papers revealed that the global phase behavior predicted for L-J fluids is qualitatively similar to that of the van der Waals equation of state, except that type VI phase behavior is also predicted. Dieters and Pegg (1989) calculated the global phase diagram for the Redlich–Kwong equation of state and found that for equal-sized molecules, the global phase diagram predicted by the Redlich–Kwong equation of state is similar to that found for the van der Waals fluid or the L-J fluid. In this case, however, no instances of type VI behavior were found. As the difference in molecular size was increased, the topology of the global phase diagram changed substantially, with new subclasses of phase behavior being predicted. Kraska and Dieters (1992) analyzed the Carnahan–Starling–Redlich–Kwong equation of state a few years later in 1992. For equal-sized molecules the results were again similar to those for the van der Waals equation of state. For molecules of different size, some unusual new phase behavior was found involving four-phase states and high-density instabilities. In recent years, a number of investigators (Scott, 1999; Wang et al., 2000; Yelash and Kraska, 1998, 1999; Yelash et al., 1999) calculated closed loops of immiscibility for equations of state based on isotropic potentials, a result that continues to be debated in the literature. Yelash and Kraska (1998) found that even a simple equation of state composed of the Carnahan–Starling repulsion and the van der Waals attraction exhibited several types of closed-loop phase behavior. One disadvantage of the global phase diagrams found in the literature is that they are based on equations of state that are applicable only for fluid phases.

In this article, we consider how including the possibility of a solid phase influences the global phase behavior of a binary mixture of equal-diameter L-J molecules. We calculate "complete" phase diagrams—that is, including solid, vapor, and liquid phases—for 29 sets of interaction parameters using the Gibbs–Duhem integration technique developed by Kofke (1993a,b). Because we used the same interaction parameters as those of Mazur et al. (1985), we are able to compare our results to their predictions for the global phase diagram of Lennard–Jones mixtures. It is important to point out that our goal is not to remap the global phase diagram because that is not our focus and is extremely expensive computationally, but instead to sample the behavior in different regions of the global phase diagram. By calculating temperature–composition phase diagrams at a number of pressures for each set of interaction parameters we are able to see how the solid phase influences the type of phase behavior exhibited by the fluid phases. That is, we seek to determine those sets of parameters for which the classification of the fluid-phase behavior with the solid phase included would differ from the classification that would be determined based solely on the fluid-phase equation of state.

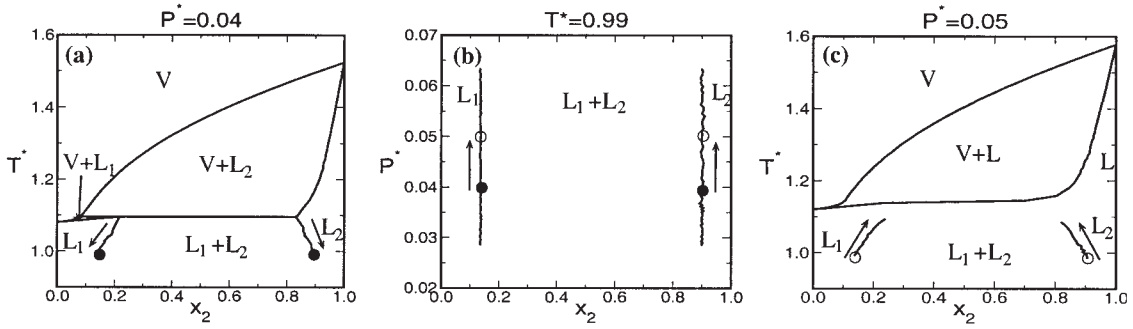

Figure 2. Method for finding liquid–liquid immiscibility with an upper critical solution temperature (UCST).

(a) Calculate a *T*–*x* diagram at low pressure. (b) Integrate with respect to pressure at constant temperature using two coexisting liquids (filled circles) found in (a) as initial conditions. (c) Conduct a second constant pressure integration using two coexisting liquids at pressure of interest (open circles) found in (b) as initial conditions.

For certain sets of parameters we consider our results in light of the classification scheme for complete phase diagrams developed by Valyashko (1986). Valyashko proposed a scheme of 12 types based on analysis of experimental data and the method of continuous topological transformation. Valyashko proposed two main groups of complete phase behavior. In group 1 systems, a continuous three-phase (SLV) curve in *P*–*T*– *x* space connects the triple points of the two components. In group 2 systems, the three-phase (SLV) curve is interrupted by the locus of L–V critical points, resulting in a discontinuity in both of the curves. Further subclasses are determined by considering the presence and location of the liquid–liquid immiscibility region and the locus of the three-phase (SLV) coexistence curve.

Highlights of our results are as follows. We find that for mixtures in which the components have similar critical temperatures, inclusion of the solid phase does not significantly alter the types of fluid-phase equilibria observed. This is because for these mixtures the melting point of both components is below the boiling point of either component. As such, the solid phase can impact only the observed vapor-phase behavior at low pressures close to the triple point of one or both of the components. Because the phase behavior classification scheme is based mainly on the locus of the vapor–liquid critical points, this low-pressure interaction does not alter the classification of these mixtures. However, as the difference in critical temperatures increases, the solid phase of the component with the higher critical temperature can coexist with the vapor phase of the component with the lower critical temperature. This results in some interesting new behavior, such as the formation of a vapor–solid eutectic point. The type of fluid-phase behavior observed when the presence of the solid phase is considered (according to the van Konynenburg classification scheme) differs from the type of fluid-phase behavior that would have been observed if the presence of the solid phase had not been considered. In other words, sometimes the fluid-phase equilibria calculated when the solid phase is not considered (such as liquid–liquid immiscibility at low temperatures) becomes metastable with respect to the solid phases when the solid phase is considered. It is seen that in those cases the solid phase effectively alters the classification of the fluid-phase behavior that would be seen in experiment from what would have been predicted based on a fluid-phase-only equation of state.

The remainder of this paper is organized as follows. In the following section we briefly review the Gibbs–Duhem technique for binary mixtures. Following that, we present our results and discuss their significance. Finally we conclude the paper with a brief summary.

Method

Gibbs–Duhem integration technique

The Gibbs–Duhem integration technique is based on integrating an appropriate form of the Clapeyron equation, which describes how the field variables vary as a function of each other at equilibrium. One can calculate the properties of two coexisting phases as a function of almost any variable of interest. For a mixture of *c* components, the Gibbs–Duhem equation (Kofke, 1993b) can be expressed as

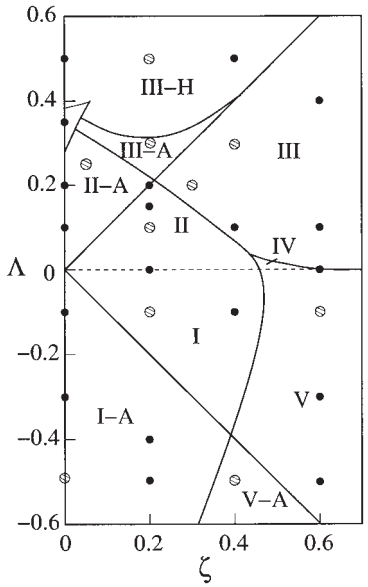

Figure 3. Global phase diagram calculated by Mazur et al. (1985) for binary mixtures.

The small solid dots indicate points in parameter space at which we calculated at least one complete phase diagram. The larger, hashed dots indicate points illustrated in Figures 4–13.

Table 1. Three-Phase Coexistence Data from the Figures Discussed

ε_{22}	ε_{12}	P^*	T^*	Phases	x_2	Figure
1.500	1.375	0.005	0.873	V-L_2-S	0.014, 0.364, 0.462	4b
			0.919	V-L_1-S	0.045, 0.524, 0.595	
		0.001425	0.715	V-L-S	0.000, 0.037, 0.087	4c
1.000	1.500	0.002	0.740	V-L-S	0.000, 0.062, 0.108	5
			0.852	V-L-S	0.052, 0.356, 0.375	
1.500	1.125	0.002	0.701	L_1-S_1-S_2	0.060, 0.117, 0.932	6
			0.736	V-L_1-S_2	0.008, 0.088, 0.924	
			1.025	V-L_2-S_2	0.803, 0.997, 0.999	
1.105	0.789	0.08	0.690	S_1-L_1-S_2	0.005, 0.012, 0.995	7a
			0.760	L_1-L_2-S_2	0.024, 0.982, 0.994	
		0.01	0.685	S_1-L_1-S_2	0.005, 0.011, 0.996	7b
			0.755	L_1-L_2-S_2	0.024, 0.982, 0.994	
			0.841	L_1-V-L_2	0.049, 0.329, 0.963	
		0.0016	0.673	S_1-V-S_2	0.007, 0.246, 0.997	7c
			0.686	S_1-L_1-V	0.001, 0.002, 0.058	
2.333	1.167	0.15	0.700	V-S_1-S_2	0.002, 0.004, 0.999	8a
			1.607	V-L_2-S_2	0.033, 0.990, 0.998	
		0.05	0.689	L_1-S_1-S_2	0.002, 0.004, 1.000	8b
			1.122	V-L_1-S_2	0.003, 0.008, 1.000	
			1.603	V-L_2-S_2	0.062, 0.996, 0.999	
		0.005	0.687	L_1-S_1-S_2	0.002, 0.004, 1.000	8c
			0.838	V-L_1-S_2	0.002, 0.007, 1.000	
			1.594	V-L_2-S_2	0.479, 0.998, 1.000	
1.857	1.143	0.10	0.688	V-S_1-S_2S	0.002, 0.004, 1.000	9
			1.257	L_1-L_2-S_2	0.093, 0.942, 0.988	
			1.283	V-L_1-L_2	0.043, 0.097, 0.932	
1.500	0.875	0.10	0.692	S_1-L-S	0.002, 0.003, 1.000	10
			1.030	L_1-L_2-S_2	0.027, 0.986, 0.997	
			1.243	L_1-V-L_2	0.116, 0.135, 0.956	
1.500	0.625	0.05	0.691	S_1-L_1-S_2	0.000, 0.001, 1.000	11
			1.033	L_1-L_2-S_2	0.005, 0.999, 1.000	
			1.104	L_1-V-L_2	0.006, 0.066, 0.998	
4.000	2.750	0.15	2.614	V-L_2-S	0.036, 0.879, 0.956	12a
		0.05	1.149	V-L_1-S	0.000, 0.002, 0.469	12b
			2.697	V-L_2-S	0.088, 0.952, 0.984	
		0.005	0.808	V-L_1-S	0.000, 0.003, 0.214	12c
			2.746	V-L_2-S	0.802, 0.999, 1.000	
2.333	2.500	0.005	0.806	V-L_1-S	0.000, 0.021, 0.126	13
			1.572	V-L_2-S	0.170, 0.684, 0.717	

*For each three-phase line the temperature, the identity of each of the phases, and their respective mole fractions of component 2, are given. Blank spaces should be interpreted as repetitions of the entry above.

$$d\ \ln\left[\sum_{i=1}^{c}\hat{f}_i\right] = h_r d\beta + Z d\ln p - \sum_{i=1}^{c}\frac{x_i}{\xi_i}d\xi_i \qquad (1)$$

where p is the pressure; Z is the compressibility factor; x_i and f_i are the mole fraction and fugacity of species i, respectively; h_r is the residual molar enthalpy; $\beta = 1/kT$, where T is temperature and k is Boltzmann's constant; and ξ_i is the fugacity fraction, defined as

$$\xi_i = \frac{\hat{f}_i}{\sum_{n=1}^{c}\hat{f}_n} \qquad (2)$$

For binary mixtures Eq. 1 reduces to the following

$$d\ \ln(\hat{f}_1 + \hat{f}_2) = h_r d\beta + Z d\ln p - \frac{x_2 - \xi_2}{\xi_2(1-\xi_2)}d\xi_2 \qquad (3)$$

given that $x_1 = 1 - x_2$ and $\xi_1 = 1 - \xi_2$.

The Gibbs–Duhem equation can be applied to two phases, α and γ, in equilibrium, by calculating Eq. 3 for each of the phases. Because the fugacity, and hence the fugacity fraction, of each of the components is identical in phases α and γ, we can set the right-hand sides of those two equations equal to obtain

$$h_r^\alpha d\beta + Z^\alpha d\ln p - \frac{x_2^\alpha - \xi_2}{\xi_2(1-\xi_2)}d\xi_2 = h_r^\gamma d\beta + Z^\gamma d\ln p - \frac{x_2^\gamma - \xi_2}{\xi_2(1-\xi_2)}d\xi_2 \qquad (4)$$

At this point one has a choice as to which variable to hold constant and which variable to integrate. In the calculation of temperature–composition diagrams we hold pressure constant and integrate Eq. 4 with respect to the fugacity fraction of component 2. Solving for $d\beta/d\xi_2$ we get

$$\frac{d\beta}{d\xi_2} = \frac{x_2^\alpha - x_2^\gamma}{(h_r^\alpha - h_r^\gamma)\xi_2(1-\xi_2)} \qquad (5)$$

By starting with values of β and ξ_2 at a known equilibrium point, we can calculate β as a function of ξ_2 for the rest of the

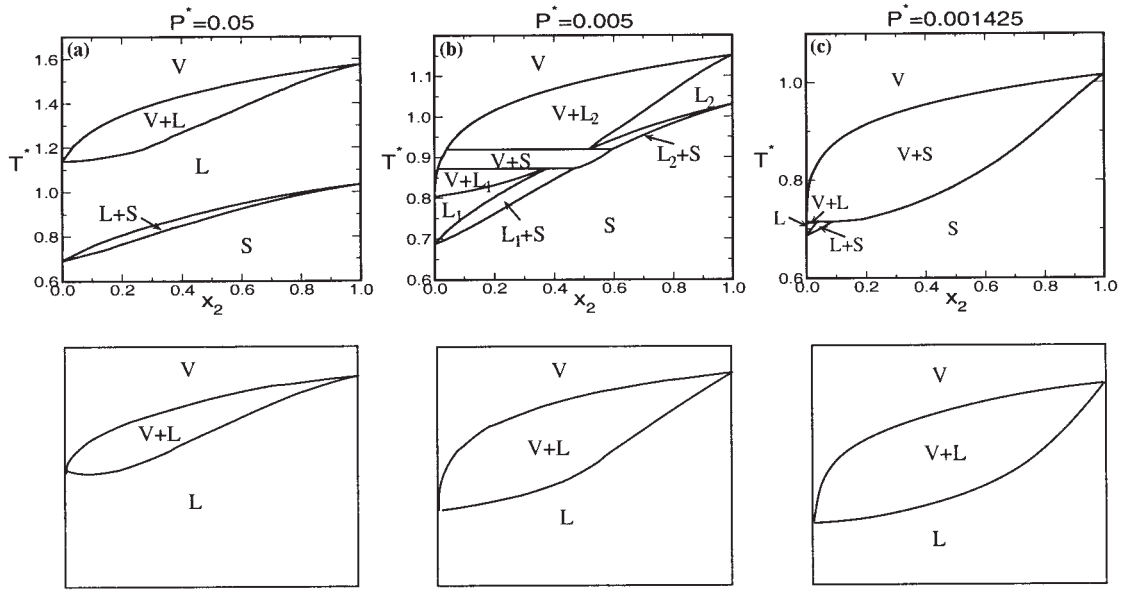

Figure 4. A series of temperature–composition diagrams.

Plots are at varying pressures for binary mixtures of equal diameter L-J atoms with $\zeta = 0.2$ and $\Lambda = -0.1$, which is in the type I region on the Mazur et al. (1985) global phase diagram. The upper row of graphs is data calculated by the Gibbs–Duhem integration technique and the lower row represents data calculated when excluding the solid phase.

coexistence curve by integrating Eq. 5. To start the integration, an initial value for the integrand is needed. In general, we start the integration at one of the pure components (that is, $\xi_2 = 0$ or 1). Because the right-hand side of Eq. 5 is undefined at either of these conditions, we obtain its value by calculating its limit as $\xi_2 \to 0$ or 1. Assuming the mixtures to be ideal as $\xi_2 \to 0$, the following approximations are made

$$\hat{f}_2 = x_2 H_2 \tag{6}$$

$$\hat{f}_1 = f_1^\circ \tag{7}$$

where f_1° is the fugacity of pure component 1; these approximations are based on Henry's law and the Lewis–Randall rule, respectively. Thus we can write

$$\left.\frac{d\beta}{d\xi_2}\right|_{\xi_2=0} = \frac{\left(\frac{f_1^\circ}{H_2}\right)^\alpha - \left(\frac{f_1^\circ}{H_2}\right)^\gamma}{h_r^\alpha - h_r^\gamma} \tag{8}$$

The quantity f_1°/H_2 can be evaluated during an NPT simulation (at the boiling temperature of pure component 1 for the desired pressure) on pure component 1 by performing trial identity switches of randomly chosen atoms. The value of f_1°/H_2 can then be calculated from

$$\frac{f_1^\circ}{H_2} = \langle \exp(\Delta U_{switch}/kT) \rangle_{NPT} \tag{9}$$

where $\langle\ \rangle$ denotes the ensemble average and U_{switch} is the potential energy change upon switching particle identities. The values of $(f_1^\circ/H_2)^\alpha$ and $(f_1^\circ/H_2)^\gamma$ can be calculated by conducting a simulation at the density of the α and γ phases, respectively. If we are starting the integration for $0 < \xi_2 < 1$, the above steps are unnecessary and we can simply use Eq. 5 to calculate the initial value of the integrand. In either case, the values of the compositions and enthalpies in Eq. 5 will either be known from a prior Gibbs–Duhem integration or can be calculated by an NPTξ_2 simulation at the desired temperature, pressure, and fugacity fraction.

Once the initial condition is calculated, the integration is carried out using a standard predictor–corrector algorithm. A step, $\Delta\xi_2$, in the fugacity fraction value is taken and the predictor formula is used to find the new value for the inverse temperature, that is

$$\beta_1 = \beta_0 + \int_{\xi_2=0}^{\xi_2=\Delta\xi_2} \frac{d\beta}{d\xi_2}\, d\xi_2 \tag{10}$$

A separate semigrand ensemble (constant NPTξ_2) Monte Carlo simulation is then performed for each of the coexisting phases to evaluate the enthalpy and composition at the new fugacity fraction and temperature. After the simulations have been equilibrated, the integrand is recalculated, the corrector formula is applied to find the "corrected" inverse temperature, and more simulations are performed at the new value for the temperature. This corrector step is repeated until the inverse temperature converges to its final value. A production run of simulations is then carried out to calculate the final values for the enthalpies and compositions of the coexisting phases. These values are then used in the predictor formula to calculate the inverse temperature at the next value of the fugacity fraction. Continuing this process we can calculate the entire phase coexistence envelope, starting at phase equilibrium for either of the pure components.

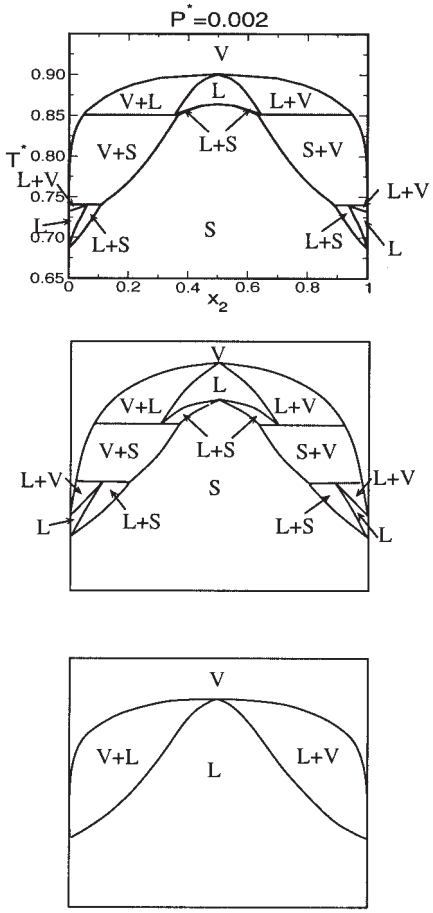

Figure 5. A temperature–composition diagram.

Conditions: pressure, $P^* = 0.002$ for binary mixtures of equal diameter L-J atoms with $\zeta = 0.0$ and $\Lambda = -0.5$, which is in the type I-A region on the Mazur et al. (1985) global phase diagram. The upper graph is data calculated by the Gibbs–Duhem integration technique, the middle graph is a schematic of the upper graph, and the lower graph is data calculated when excluding the solid phase.

For certain sets of parameters, there is a range of pressures for which two two-phase coexistence envelopes (such as vapor–liquid and liquid–solid) overlap over a range of temperatures resulting in three-phase equilibria (such as vapor–liquid–solid coexistence) at the point of intersection. A new type of two-phase equilibria (such as solid–vapor) will occur in the range of temperatures for which the envelopes overlap. The solid–vapor coexistence envelope is calculated by conducting a Gibbs–Duhem integration starting at the values of temperature and ξ_2 at the point of overlap of the vapor–liquid and liquid–solid coexistence envelopes. The solid and vapor phases at that temperature are used as the initial coexisting phases to start the integration. This procedure is explained in greater detail in an article by Lamm and Hall (2001).

A different approach is needed to calculate low-temperature liquid–liquid immiscibility with an upper critical solution temperature (UCST), as would be found in type II phase behavior at higher pressures, because those curves do not originate at either of the pure components. One way to calculate an initial point for starting the integration would be to use Gibb's ensemble simulation to calculate the properties of the coexisting liquids at one temperature. We have developed an alternative approach that makes use of the Gibbs–Duhem integration technique, as illustrated in Figure 2 for the system $\zeta = 0.2$ and $\Lambda = 0.175$. Our approach starts by calculating a temperature–composition diagram at a pressure ($P^* = 0.04$) lower than the desired pressure, where there is three-phase coexistence (Figure 2a). We then choose a temperature ($T^* = 0.99$) below the three-phase coexistence temperature at which two liquids are in equilibrium (solid circles in Figure 2a). After that a Gibbs–Duhem pressure integration can be conducted at constant temperature ($T^* = 0.99$) up to the pressure ($P^* = 0.05$) of interest (open circles Figure 2b) using the following form of the Clapeyron equation

$$\frac{dP^*}{d\xi_2} = \frac{x_2^\alpha - x_2^\gamma}{(Z^\alpha - Z^\gamma)\xi_2(1-\xi_2)} \tag{11}$$

The resulting two coexisting liquid state points can then be used as initial conditions (open circles in Figure 2c) for calculating the remainder of the liquid–liquid immiscibility curve.

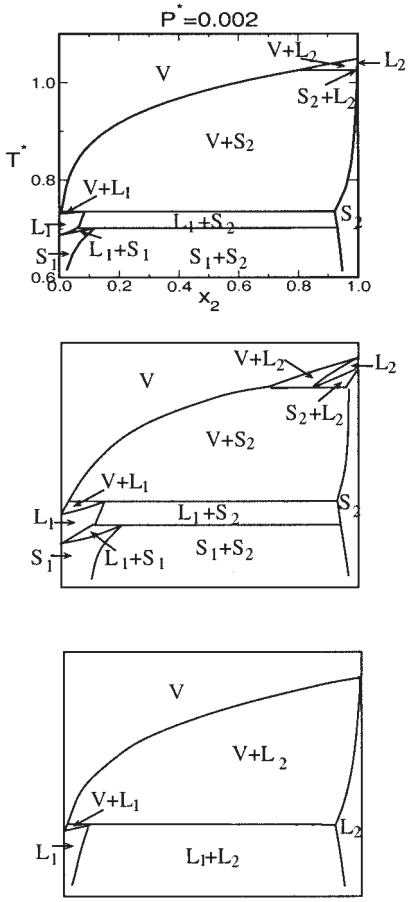

Figure 6. A temperature–composition diagram.

Conditions: pressure, $P^* = 0.002$ for binary mixtures of equal diameter L-J atoms with $\zeta = 0.2$ and $\Lambda = 0.1$, which is in the type II region on the Mazur et al. (1985) global phase diagram. The upper graph is data calculated by the Gibbs–Duhem integration technique, the middle graph is a schematic of the upper graph, and the lower graph is data calculated when excluding the solid phase.

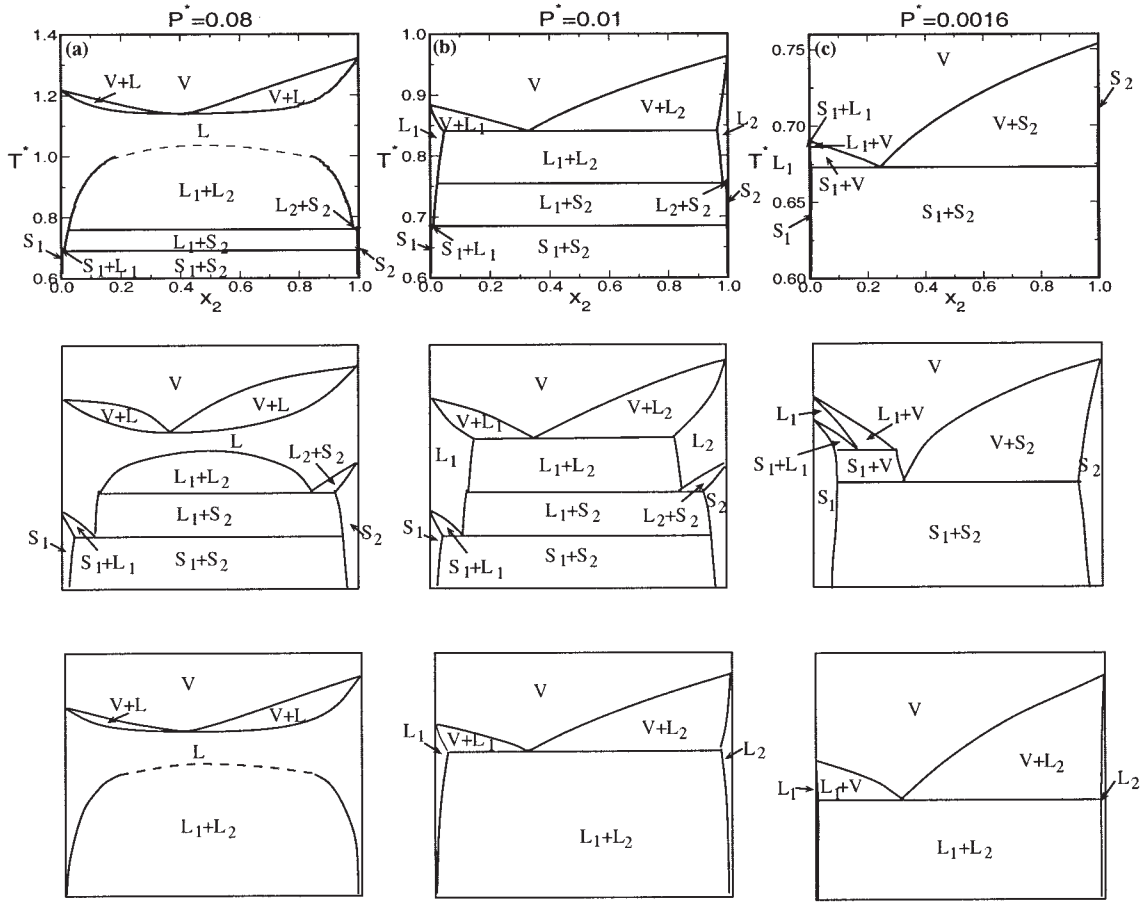

Figure 7. A series of temperature–composition diagrams.

Plots are at varying pressures for binary mixtures of equal diameter L-J atoms with $\zeta = 0.05$ and $\Lambda = 0.25$, which is in the type II-A region on the Mazur et al. (1985) global phase diagram. The upper row of graphs is data calculated by the Gibbs–Duhem integration technique, the middle row of graphs is schematics of the upper graph, and the lower row of graphs is data calculated when excluding the solid phase.

Simulations

As mentioned previously, semigrand ensemble Monte Carlo (NPTξ_2) simulations are used to evaluate the properties of the coexisting phases during the integration of the Gibbs–Duhem equation. In this section, we briefly describe how these simulations are conducted.

There are three types of moves in the semigrand ensemble: particle displacement, volume change, and identity exchange. The particle displacement and volume change moves are carried out in the same manner as in isothermal–isobaric (NPT) simulations. The identity exchange move involves choosing a random molecule in the system and switching its identity. The change in the configurational energy of the system caused by the identity change is then evaluated. The overall acceptance probability $\mathcal{P}$ for these moves is

$$\mathcal{P} = \min\left\{1, \exp\left[-\beta(U^{trial} - U^{old}) - \beta P(V^{trial} - V^{old}) + N \ln \frac{V^{trial}}{V^{old}} + \ln \frac{\xi_{trial}}{\xi_{old}}\right]\right\} \quad (12)$$

where U^{trial} and U^{old} are the configurational energies and V^{trial} and V^{old} are the volumes of the trial and existing states, respectively; N is the total number of molecules; and ξ_{trial} and ξ_{old} refer to the fugacity fractions of the trial and existing identities of the molecule during the identity exchange moves. At each step, the type of move is randomly chosen with a weighting such that for every volume change move there are 20 particle displacements and 20 identity exchange moves. After an appropriate number of equilibrium moves, running averages of the composition and enthalpy (as calculated by $h = U/N + PV/N$) are calculated for use in evaluating the integrand in the Gibbs–Duhem technique.

Other details of the simulation are as follows. Prior theoretical calculations (Cottin, 1996) and molecular simulations (Kranendonk and Frenkel, 1991) have shown that by choosing diameter ratios $0.85 \leq \sigma_{11}/\sigma_{22} \leq 1.0$ we can assume that the most stable configuration for the solid phase will be that of a substitutionally disordered fcc lattice. By using an fcc lattice as an initial configuration for the solid phase, an fcc lattice will be maintained in the solid phase throughout the simulation without any additional constraints on the simulation. The simulations are performed on a system of 500 molecules in a cubic box with periodic boundary conditions. The molecules interact by the Lennard–Jones potential

$$u_{ij}(r) = 4\varepsilon_{ij}\left[\left(\frac{\sigma_{ij}}{r}\right)^{12} - \left(\frac{\sigma_{ij}}{r}\right)^{6}\right] \quad (13)$$

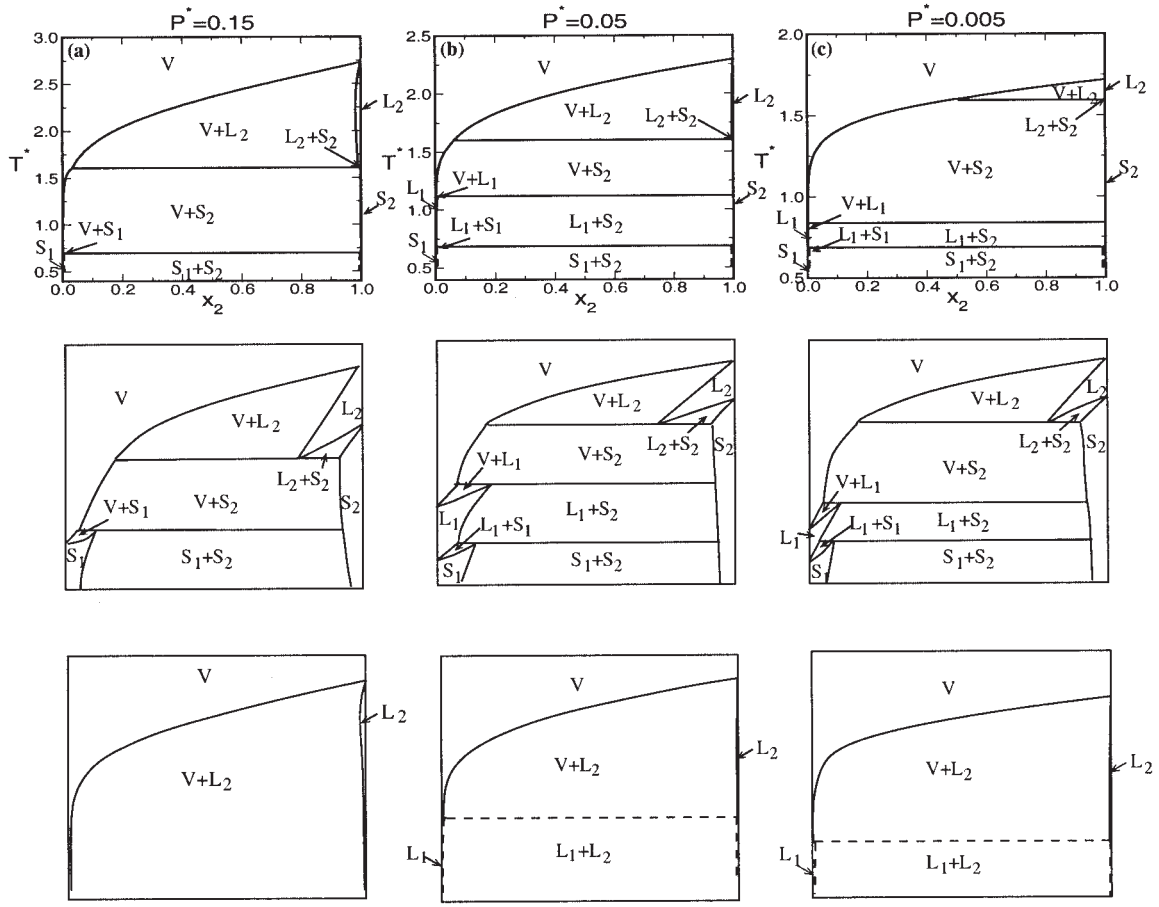

Figure 8. A series of temperature–composition diagrams.

Plots are at varying pressures for binary mixtures of equal diameter L-J atoms with $\zeta = 0.4$ and $\Lambda = 0.3$, which is in the type III region on the Mazur et al. (1985) global phase diagram. The upper row of graphs is data calculated by the Gibbs–Duhem integration technique, the middle row of graphs is schematics of the upper graph, and the lower row of graphs is data calculated when excluding the solid phase.

where u_{ij} is the potential energy of the interaction between atoms i and j, r is the distance between atoms i and j, ε_{ij} is the Lennard–Jones well depth, and σ_{ij} is the Lennard–Jones diameter. The potential interactions are truncated at half the box length and standard long-range corrections (Allen and Tildesley, 1997) are applied to the potential energy and pressure calculations.

Results and Discussion

We have calculated complete phase diagrams at conditions indicated by the circles on the Mazur et al. global phase diagram shown in Figure 3. The small dots indicate sets of parameters at which complete phase diagrams have been calculated for at least one pressure and the larger dots indicate sets of parameters at which complete phase diagrams have been calculated at more than one pressure. The parameters used in the global phase diagram are defined as

$$\zeta \equiv \frac{\varepsilon_{22} - \varepsilon_{11}}{\varepsilon_{11} + \varepsilon_{22}} \tag{14}$$

and

$$\Lambda \equiv \frac{\varepsilon_{11} + \varepsilon_{22} - 2\varepsilon_{12}}{\varepsilon_{11} + \varepsilon_{22}} \tag{15}$$

We have not calculated the phase behavior in region IV because that region is very small. In addition, it is difficult to be sure that a chosen set of parameters will lie within the Mazur et al. region IV because their global phase diagram is based on an approximate equation of state.

In each of the phase diagrams presented here, the upper row of diagrams shows the phase behavior calculated using the Gibbs–Duhem technique for the fluid and solid phases; the middle row (when present) is a schematic of the upper row of diagrams presented to show the topology of the phase behavior, which may be hard to see in the diagram containing the actual data; and the bottom row shows the phase behavior calculated when considering only the fluid phases. The fluid-phase-only diagrams were calculated by simply omitting the calculation of the solid–fluid phase coexistence. In this way we are able to calculate metastable fluid-phase equilibria below the freezing point of the mixtures. In the fluid-phase-only diagrams, the dotted lines indicate portions of the diagram whose presence is inferred rather than calculated. In these cases the fluid phase

was sufficiently unstable, compared to the solid phase, that it spontaneously solidified during the simulation. To make the diagrams easier to follow, solid curves were used to connect the data points rather than just the individual points that resulted from our calculations. The resolution of the diagrams is fairly fine and the difference in composition between two calculated points was generally less (sometimes much less) than 0.02. Table 1 lists the temperature and compositions of the coexisting phases for each of the three-phase coexistence lines found in Figures 4–13. In both the figures and the table $P^* \equiv P\sigma_{11}^3/\varepsilon_{11}$ and $T^* \equiv kT/\varepsilon_{11}$.

Figure 4 shows a series of temperature–composition phase diagrams at decreasing pressures for $\zeta = 0.2$ and $\Lambda = -0.1$, which is in the type I region on the Mazur et al. global phase diagram. In terms of the fluid-phase-only phase behavior classification, type I phase behavior is characterized by a single vapor–liquid phase coexistence envelope terminated at either end by the pure component boiling points at the pressure of interest. We find that at high pressures (such as $P^* = 0.05$, Figure 4a), the solid does not affect the fluid-phase equilibria because the vapor–liquid phase coexistence envelope occurs at a significantly higher temperature than the solid–liquid phase coexistence envelope. At intermediate pressures (such as $P^* = 0.005$, Figure 4b), the solid–liquid phase coexistence envelope intersects with the descending vapor–liquid phase coexistence envelope and a pair of three-phase lines (VL_2S and VL_1S) are formed, which separate regions of vapor–liquid, liquid–solid, and vapor–solid phase coexistence. Between these two three-phase lines lies a range of temperatures at which there is coexistence between a solid phase and a vapor phase. As the pressure decreases further, the range of temperatures at which vapor–solid equilibria occurs broadens until the triple point pressure of pure component 2 ($P^* = 0.00165$) is reached. Below this there is no longer solid–liquid and vapor–liquid equilibria for pure component 2, but only solid–vapor equilibria. At low pressures (such as $P^* = 0.001425$, Figure 4c), which is below the triple point pressure of component 2, the phase coexistence is predominantly solid–vapor. Without including the possibility of a solid phase, we would be unable to see any of the three-phase (SLV) coexistence curves in region I. The complete phase behavior can be classified as type 1a according to Valyashko's scheme, based on examining the temperature–composition phase diagrams shown in Figure 4. An experimental system that has similar complete phase behavior is silver nitrate + water (Findlay, 1951).

Figure 5 shows a temperature–composition phase diagram at $P^* = 0.002$ for $\zeta = 0.0$ and $\Lambda = -0.5$, which is in the type I-A region on the Mazur et al. global phase diagram. Because the mixture is symmetric ($a_{11} = a_{22}$) the diagram is symmetric about $x_2 = 0.5$. In terms of fluid-phase-only phase behavior classification, type I-A differs from type I, in that type I-A exhibits an azeotrope in the vapor–liquid phase coexistence envelope. When including the solid phase, we find that there is an azeotrope in the solid–liquid phase coexistence envelope as well. Because of the presence of the azeotrope there are two regions of vapor–solid phase coexistence, in contrast with the single region of vapor–solid phase coexistence seen in Figures 4a and b.

Figure 6 shows a temperature–composition phase diagram at $P^* = 0.002$ for $\zeta = 0.2$ and $\Lambda = 0.1$, which is in the type II region on the Mazur et al. global phase diagram. In terms of

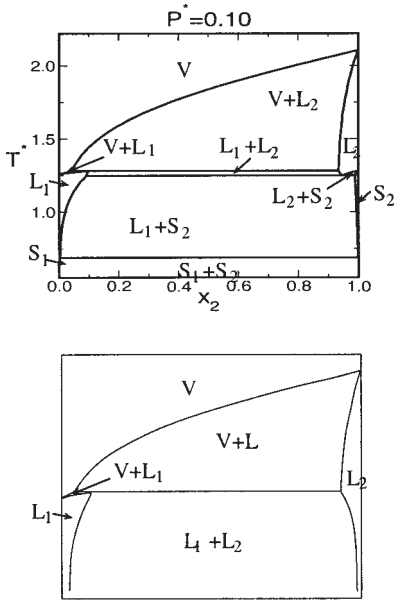

Figure 9. A temperature–composition diagram.

Conditions: pressure, $P^* = 0.10$ for binary mixture of equal diameter L-J atoms with $\zeta = 0.3$ and $\Lambda = 0.2$, which is in the type III region on the Mazur et al. (1985) global phase diagram. The upper graph is data calculated by the Gibbs–Duhem integration technique and the lower graph is data calculated when excluding the solid phase.

fluid-phase-only phase behavior classification, the fluid-phase equilibria is similar to that of type I except that type II has low-temperature liquid–liquid immiscibility. The pressure $P^* = 0.002$ is just above the triple point of component 2. Two three-phase coexistence lines (VL_2S_2 and VL_1S_2) separate regions of vapor–liquid and liquid–solid coexistence from a region of vapor–solid coexistence, whereas one three-phase coexistence line ($L_1S_1S_2$) separates regions of liquid–solid coexistence from the region of solid–solid coexistence. It can be seen that for this set of parameters and at this particular pressure and temperature, liquid–liquid immiscibility is metastable compared to the liquid–solid and solid–solid phase equilibria because liquid–liquid immiscibility is present in the fluid-phase-only diagram, but not in the complete phase diagram. The most stable phases are determined using the boundary curvature rule. The boundary curvature rule uses arguments based on the shape of the Gibbs–free energy vs. composition curve, the details of which are beyond the scope of this communication (Gordon, 1983).

Figure 7 shows a series of temperature–composition phase diagrams at decreasing pressures for $\zeta = 0.05$ and $\Lambda = 0.25$, which is in the type II-A region on the Mazur et al. global phase diagram. In terms of the fluid-phase-only phase behavior classification, type II-A phase behavior is the same as type II, with the addition of an azeotrope in the vapor–liquid coexistence curves. At the highest pressure ($P^* = 0.08$, Figure 7a) we can see that below $T^* = 0.755$ the liquid–liquid immiscibility becomes less stable than liquid–solid phase coexistence. The interference between the solid phase and liquid phases results in the formation of two three-phase coexistence lines ($L_1L_2S_2$) and ($S_1L_1S_2$) separating liquid–liquid, liquid–solid, and solid–solid phase coexistence. We are unable to calculate the liquid–

liquid immiscibility curve all the way up to the UCST because as the critical point is approached, density fluctuations cause the simulation to become unstable. The dashed line indicates where we expect the curve would be, approximately. The liquid–liquid coexistence curves in this case were calculated by the method described earlier in the Method section. As the pressure is lowered ($P^* = 0.01$, Figure 7b) the vapor–liquid coexistence envelope interferes with the liquid–liquid coexistence curves and a third three-phase line (L_1VL_2) is produced. As the pressure decreases further the L_1VL_2 line decreases in temperature and the $L_1L_2S_2$ increases in temperature until they eventually coincide to form a four-phase ($L_1VL_2S_2$) line at one value of the pressure (the quadruple point). We have not located the quadruple point directly because this involves guessing the exact temperature at which it occurs. [An alternative approach would be to conduct two Gibbs–Duhem integrations along the two three-phase lines (L_1VL_2 and $L_1L_2S_2$) to find the pressure at which they merge. This is beyond the scope of this article.] At the lowest pressure shown ($P^* = 0.00116$, Figure 7c), which is below the triple point of component 2, there are two three-phase lines: (S_1L_1V) and (S_1VS_2). The

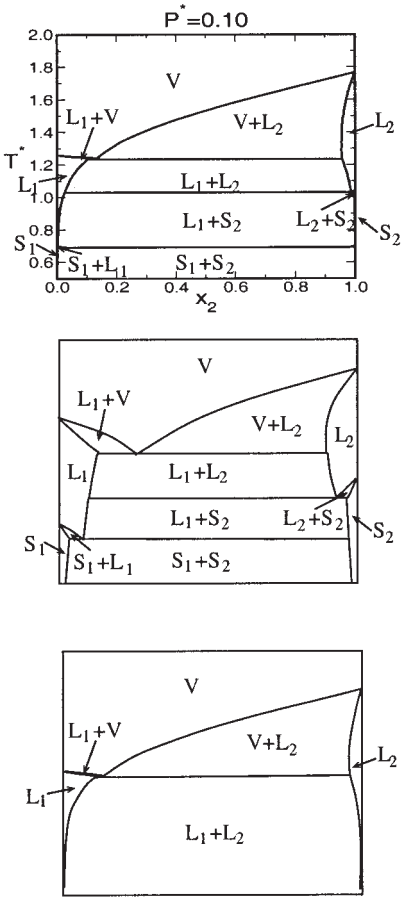

Figure 10. A temperature–composition diagram.

Conditions: pressure, $P^* = 0.10$ for binary mixtures of equal diameter L-J atoms with $\zeta = 0.2$ and $\Lambda = 0.3$, which is in the type III-A region on the Mazur et al. (1985) global phase diagram. The upper graph is data calculated by the Gibbs–Duhem integration technique, the middle graph is a schematic of the upper graph, and the lower graph is data calculated when excluding the solid phase.

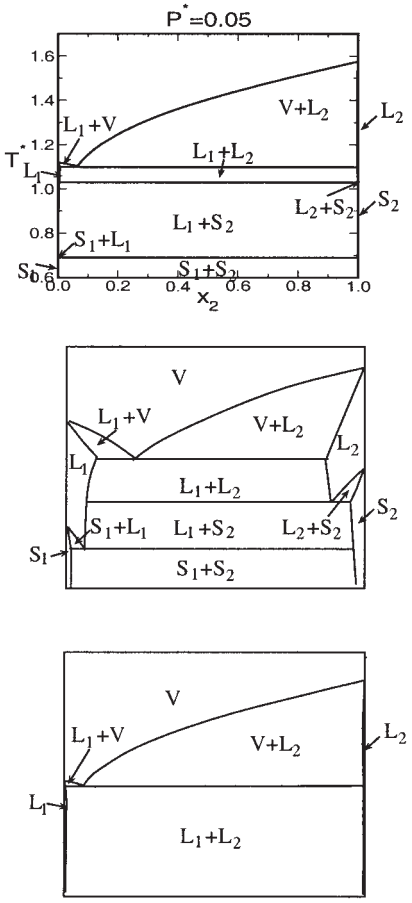

Figure 11. A temperature–composition diagram.

Conditions: pressure, $P^* = 0.05$ for binary mixtures of equal diameter L-J atoms with $\zeta = 0.2$ and $\Lambda = 0.5$, which is in the type III-H region on the Mazur et al. (1985) global phase diagram. The upper graph is data calculated by the Gibbs–Duhem integration technique, the middle graph is a schematic of the upper graph, and the lower graph is data calculated when excluding the solid phase.

liquid–liquid immiscibility has been completely preempted by the presence of the solid phase. In addition, a solid–vapor eutectic point, a vapor in equilibrium with two solid phases, has been formed. The interesting phenomena here are the changes in the three-phase lines as the pressure decreases and the formation of a vapor–solid eutectic point, neither of which would be seen without including the possibility of the solid phase. The complete phase behavior can most closely be classified as type 1b′ according to Valyashko's scheme based on examining the temperature–composition phase diagrams shown in Figure 7. Based on the series of phase diagrams shown in Figure 7, the experimental system ethane + *n*-tetracosane exhibits the most similar phase behavior, although there is no azeotrope in the vapor–liquid phase equilibria (Peters et al., 1986).

Figure 8 shows a series of temperature–composition phase diagrams at decreasing pressures for $\zeta = 0.4$ and $\Lambda = 0.3$, which is in the type III region on the Mazur et al. global phase diagram. In terms of the fluid-phase-only phase behavior classification, type III phase behavior differs from types I and II in that there is not a continuous locus of critical points from one

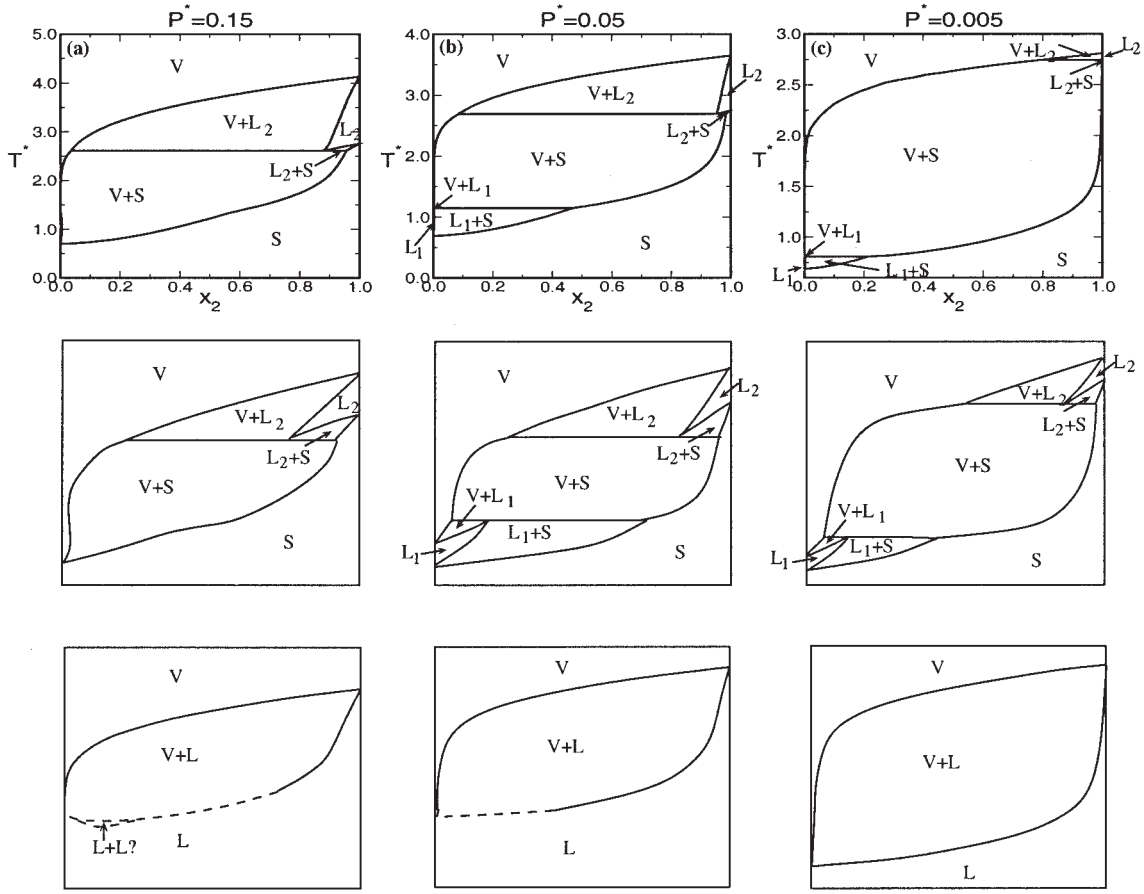

Figure 12. A series of temperature–composition diagrams.

Plots are at varying pressures for binary mixtures of equal diameter L-J atoms with $\zeta = 0.6$ and $\Lambda = -0.1$, which is in the type V region on the Mazur et al. (1985) global phase diagram. The upper row of graphs shows data calculated by the Gibbs–Duhem integration technique, the middle row of graphs are schematics of the upper graph, and the lower row of graphs shows data calculated when excluding the solid phase.

pure component critical point to the other. At the highest pressure ($P^* = 0.15$, Figure 8a), which is above the critical pressure of pure component one, we see that the interference of the solid phase with the vapor–liquid equilibria results in two three-phase coexistence lines (VL_2S2 and VS_1S_2) separating regions of vapor–liquid, vapor–solid, and solid–solid phase coexistence. At the two lower pressures ($P^* = 0.05$, Figure 8b and $P^* = 0.005$, Figure 8c), which are below the critical pressure of component 2, a third three-phase coexistence line (VL_1S_2) is formed and liquid–solid phase coexistence appears. One feature of type III phase behavior that we do not see in this series of graphs is liquid–liquid immiscibility. Because the melting point of component 2 is above the boiling point of component 1, we find liquid–solid and solid–solid phase coexistence occurring in the region where we would have expected liquid–liquid immiscibility. We did, however, find a small set of parameter sets in the type III region where liquid–liquid immiscibility was not completely hidden by the liquid–solid and solid–solid phase equilibria. Figure 9 is one such set of parameters, with $\zeta = 0.3$ and $\Lambda = 0.2$. It can be seen that for a narrow range of temperature there are two liquids in equilibrium with each other. We could not find a set of parameters in the type III region in which the UCST of the liquid–liquid immiscibility was stable with respect to the solid–liquid and solid–solid phase equilibria. The complete phase behavior can most closely be classified as type 2a according to Valyashko's scheme based on examining the temperature–composition phase diagrams shown in Figure 8. An experimental system that has similar complete phase behavior is sodium sulfate and water (Findlay, 1951).

Figure 10 shows a temperature–composition phase diagram at $P^* = 0.10$ for $\zeta = 0.2$ and $\Lambda = 0.3$, which is in the type III-A region on the Mazur et al. global phase diagram. In terms of the fluid-phase-only phase behavior classification, type III-A phase behavior is distinguished from type III by the presence of an azeotrope in the vapor–liquid phase diagram at high pressures. It can be seen in Figure 10, that the interference of the solid phase with the vapor–liquid equilibrium results in the formation of two additional three-phase coexistence lines ($L_1L_2S_2$ and $S_1L_1S_2$) separating regions of liquid–liquid, liquid–solid, and solid–solid phase equilibria. Although we investigated the phase behavior at a number of different pressures, we never located a UCST for the liquid–liquid immiscibility, which indicates that this set of parameters may actually be in the type III-H region.

Figure 11 shows a temperature–composition phase diagram at $P^* = 0.05$ for $\zeta = 0.2$ and $\Lambda = 0.5$, which is in the type III-H region on the Mazur et al. global phase diagram. In terms of the

fluid-phase-only phase behavior classification, type III-H phase behavior is distinguished from type III by the presence of a heteroazeotrope in the vapor–liquid phase diagram, that is, a vapor–liquid eutectic. It differs from type III-A in the following way. Although type III-A also has a heteroazeotrope at low pressure, as the pressure is increased the vapor–liquid equilibria separates from the liquid–liquid equilibria and the heteroazeotrope is replaced by an azeotrope. In type III-H phase equilibria, the heteroazeotrope is not replaced by an azeotrope at any pressure. In this figure we can see that the increased value of Λ compared to that in Figure 10 (that is, decreased attractions between the two components) has caused the two components to become more immiscible.

Figure 12 shows a series of temperature–composition phase diagrams at decreasing pressures for $\zeta = 0.6$ and $\Lambda = -0.1$, which is in the type V region on the Mazur et al. global phase diagram. In terms of the fluid-phase-only phase behavior classification, the unique feature of type V phase behavior is a region of liquid–liquid immiscibility with a lower critical solution temperature (LCST) below the vapor–liquid coexistence envelope, as depicted by the dashed lines in the bottom T– x diagram at $P^* = 0.15$ (Figure 12a). However, we found that the presence of the solid phase preempted the appearance of liquid–liquid immiscibility. The consequence of this is that, although the equation of state might predict that this system should exhibit type V phase behavior, experimentally it would appear to behave more like a type I mixture. As indicated in the fluid-phase-only diagrams by the dashed line, we were unable to calculate the complete fluid phase coexistence envelopes at the two highest pressures. This occurred because the coexisting vapor and liquid phases became so unstable as the vapor–solid coexistence region was entered during our simulations, that the liquid phase spontaneously crystallized resulting in coexisting vapor and solid phases. This prevented us from confirming the existence of the liquid–liquid immiscibility expected for type V phase behavior. Similar attempts to find the LCST at $\zeta = 0.6$ and $\Lambda = -0.3$ or $\Lambda = -0.5$ were also unsuccessful. The complete phase behavior can be classified as type 2a according to Valyashko's scheme, based on examining the temperature–composition phase diagrams shown in Figure 12. According to Garcia and Luks (1999) an experimental example of a system that exhibits similar phase behavior is carbon dioxide + n-tetracosane.

Figure 13 shows a temperature–composition phase diagram at $P^* = 0.005$ for $\zeta = 0.4$ and $\Lambda = -0.5$, which is in the type V-A region on the Mazur et al. global phase diagram. In terms of the fluid-phase-only phase behavior classification, type V-A phase behavior is similar to type V phase behavior, with the additional feature of an azeotrope in the vapor–liquid phase coexistence envelope. In Figure 13, it can be seen that there is an azeotrope in both the vapor–liquid and solid–liquid phase coexistence envelopes. Furthermore, we see that the interference of the solid phase with the vapor–liquid equilibria results in two three-phase coexistence lines (VL_2S and VL_1S) separating regions of vapor–liquid, vapor–solid, and liquid–solid phase coexistence.

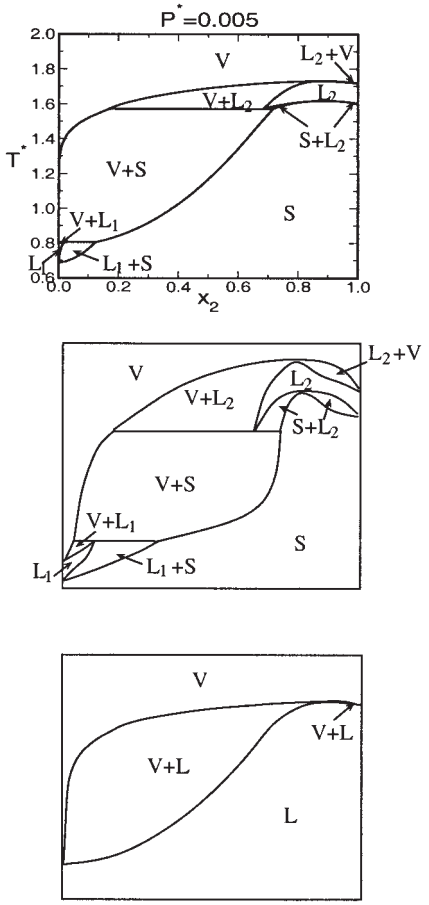

Figure 13. A temperature–composition diagram.

Conditions: pressure, $P^* = 0.005$ for binary mixtures of equal diameter L-J atoms with $\zeta = 0.4$ and $\Lambda = -0.5$, which is in the type V-A region on the Mazur et al. (1985) global phase diagram. The upper graph is data calculated by the Gibbs–Duhem integration technique, the middle graph is a schematic of the upper graph, and the lower graph is data calculated when excluding the solid phase.

Summary and Conclusions

Our general conclusions are that for mixtures in which the components have similar critical temperatures (that is, $\zeta <$ 0.3), inclusion of the solid phase does not alter how the phase behavior of the mixture would be classified based solely on the fluid-phase behavior. This is because the classification scheme is based primarily on the locus of gas phase critical points. For values of ζ close to zero, the influence of the solid phase is felt only at temperatures and pressures well below the critical point of either species, which means that it does not alter the topology of the locus of critical points. This is seen to be especially true in regions I and II. For mixtures in which the components have greatly dissimilar critical temperatures (that is, $\zeta > 0.4$), the fluid-phase behavior type may be different from what is expected because the solid phase for the component with the higher critical point can exist in equilibrium with supercritical phases of the other component. When this happens, the coexistence between a vapor rich in one species and a solid rich in the other species can alter the topology of the locus of vapor–liquid critical points. This was seen in the figures presented for region V.

The Gibbs–Duhem integration technique was used to calculate composition–temperature phase diagrams at 29 different points on the global phase diagram for binary mixtures of

Lennard–Jones molecules. We presented phase diagrams calculated in each region of the global phase diagram, with the exception of region IV. We compared our results to the global phase diagram calculated by Mazur et al. using a polynomial equation of state for binary mixtures of Lennard–Jones molecules. We found that for mixtures of components with similar critical temperatures (that is, $\zeta < 0.3$), the phase behavior was essentially the same as in the fluid-phase-only case. For mixtures in which the components had greatly dissimilar critical temperatures, $\zeta > 0.4$, interaction between the vapor and solid phases could significantly alter the fluid-only phase behavior. This was manifested in interesting types of solid–fluid phase behavior, such as a vapor–solid eutectic point, that is, a vapor in equilibrium with two immiscible solids. We found that a mixture that would be expected to have type V phase behavior according to a fluid-phase equation of state might experimentally exhibit type I phase behavior. This is because the phase behavior features unique to type V phase behavior occur below the freezing point of the mixtures. We also found that, although the Gibbs–Duhem integration technique does make it possible to calculate metastable phase behavior below the freezing point of the mixtures, the calculations are limited by the stability of the coexisting metastable phases.

Acknowledgments

This work was supported by the Office of Energy Research, Basic Energy Sciences, Chemical Sciences Division of the U.S. Department of Energy under Contract No. DE-FG02-97ER14771. Acknowledgment is also made to the Donors of the Petroleum Research Fund administered by the American Chemical Society for partial support of this work.

Literature Cited

Allen, M. P., and D. J. Tildesley, *Computer Simulation of Liquids.* Oxford Science Publications, Oxford, U.K. (1997).

Boshkov, L. Z., "On the Description of Closed-Loop Phase Diagrams of 2-Component Solutions, Based in the One-Fluid Equation of State," *Dokl. Akad. Nauk SSSR*, **294**, 901 (1987).

Boshkov, L. Z., and V. A. Mazur, "Phase Equilibria and Critical Lines of Lennard–Jones Molecules in Binary Mixtures," *Russ. J. Phys.*, **60**, 16 (1986).

Cottin, X., "A Theoretical Study of the Thermodynamics of Solid Solutions and Solid–liquid Phase Equilibria," PhD Thesis, University of Massachusetts, Amherst (1996).

Deiters, U. K., and I. L. Pegg, "Systematic Investigation of the Phase-Behavior in Binary Fluid Mixtures. I. Calculations Based on the Redlich–Kwong Equation of State," *J. Chem. Phys.*, **90**, 6632 (1989).

Ericsson, B., and B. Hallmans, "Treatment of Saline Wastewater for Zero Discharge at the Debiensko Coal Mines in Poland," *Desalination*, **105**, 115 (1996).

Findlay, A., *The Phase Rule*, 9th edition, Dover Publications, New York (1951).

Furman, D., S. Dattagupta, and R. B. Griffiths, "Global Phase Diagram for a Three-Component Model," *Phys. Rev. B*, **15**, 441 (1977).

Furman, D., and R. B. Griffiths, "Global Phase Diagram for a van der Waals Model of a Binary Mixture," *Phys. Rev. A*, **17**, 1139 (1978).

Garcia, D. C., and K. D. Luks, "Patterns of Solid–Fluid Phase Equilibria: New Possibilities?," *Fluid Phase Equil.*, **161**, 91 (1999).

Gordon, P., *Principles of Phase Diagrams in Material Systems*, McGraw-Hill, New York (1983).

Kofke, D. A., "Direct Evaluation of Phase Coexistence by Molecular Simulation via Integration Along the Saturation Line," *J. Chem. Phys.*, **98**, 4149 (1993a).

Kofke, D. A., "Gibbs–Duhem Integration: A New Method for Direct Evaluation of Phase Coexistence by Molecular Simulation," *Mol. Phys.*, **78**, 1331 (1993b).

Kramer, H. J. M., and P. J. Jansens, "Tools for Design and Control of Industrial Crystallizers—State of the Art and Future Needs," *Chem. Eng. Technol.*, **26**, 247 (2003).

Kranendonk, W. G. T., and D. Frenkel, "Computer Simulation of Solid–Liquid Coexistence in Binary Hard-Sphere Mixtures," *Mol. Phys.*, **72**, 679 (1991).

Kraska, T., and U. K. Deiters, "Systematic Investigation of the Phase Behavior in Binary Fluid Mixtures. II. Calculations Based on the Carnahan–Starling–Redlich–Kwong Equation of State," *J. Chem. Phys.*, **96**, 539 (1992).

Lamm, M. H., and C. Hall, "Molecular Simulation of Complete Phase Diagrams in Binary Mixtures," *AIChE J.*, **47**, 1664 (2001).

Mazur, V. A., L. Z. Boshkov, and V. B. Fedorov, "Phase Equilibria in 2-Component Lennard–Jones Systems," *Dokl. Akad. Nauk SSSR*, **282**, 137 (1985).

Peters, C. J., R. N. Lichtenthaler, and J. de Swaan Arons, "Three Phase Equilibria in Binary Mixtures of Ethane and Higher N-Alkanes," *Fluid Phase Equil.*, **29**, 495 (1986).

Ree, F. H., "Analytic Representation of Thermodynamic Data for Lennard–Jones Fluids," *J. Chem. Phys.*, **73**, 5401 (1980).

Schroer, J. W., C. Wibowo, and K. M. Ng, "Synthesis of Chiral Crystallization Processes," *AIChE J.*, **47**, 369 (2001).

Scott, R. L., "Van der Waals-like Global Phase Diagrams," *Phys. ChE. Chem. Phys.*, **1**, 4225 (1999).

Valyashko, V. M., "Complete Phase Diagrams of Binary Systems with Different Volatility Components," *Z. Phys. Chem.*, **267**, 481 (1986).

van Konynenburg, P. H., "Critical Lines and Phase Equilibria in Binary Mixtures," PhD Thesis, University of California, Los Angeles (1968).

van Konynenburg, P. H. and R. L. Scott, "Van Der Waals Mixtures," *Discuss. Faraday Soc.*, **49**, 87 (1970).

van Konynenburg, P. H., and R. L. Scott, "Critical Lines and Phase Equilibria in Binary van der Waals Mixtures," *Philos. Trans. R. Soc. Lond., Ser. A Phys Sci*, **298**, 495 (1980).

Wang, J.-L., G.-W. Wu, and R. J. Sadus, "Closed-Loop Liquid–Liquid Equilibria and the Global Phase Behavior of Binary Mixtures Involving Hard-sphere and van der Waals Interactions," *Mol. Phys.*, **98**, 715 (2000).

Yelash, L. V., and T. Kraska, "Closed-Loops of Liquid–Liquid Immiscibility in Binary Mixtures of Equal Sized Molecules Predicted with a Simple Theoretical Equation of State," *Ber. Unsenges Phys. Chem.*, **102**, 213 (1998).

Yelash, L. V., and T. Kraska, "On Closed-Loop Liquid–Liquid Immiscibility," *Phys. ChE. Chem. Phys.*, **1**, 307 (1999).

Yelash, L. V., T. Kraska, and U. K. Deiters, "Closed-Loop Critical Curves in Simple Hard-Sphere van der Waals-Fluid Models Consistent with the Packing Fraction Limit," *J. Chem. Phys.*, **110**, 3079 (1999).

Manuscript received July 30, 2003, and revision received Nov. 3, 2003.